

# (1) 9 The structure and characteristic scales of the H I gas in galactic disks

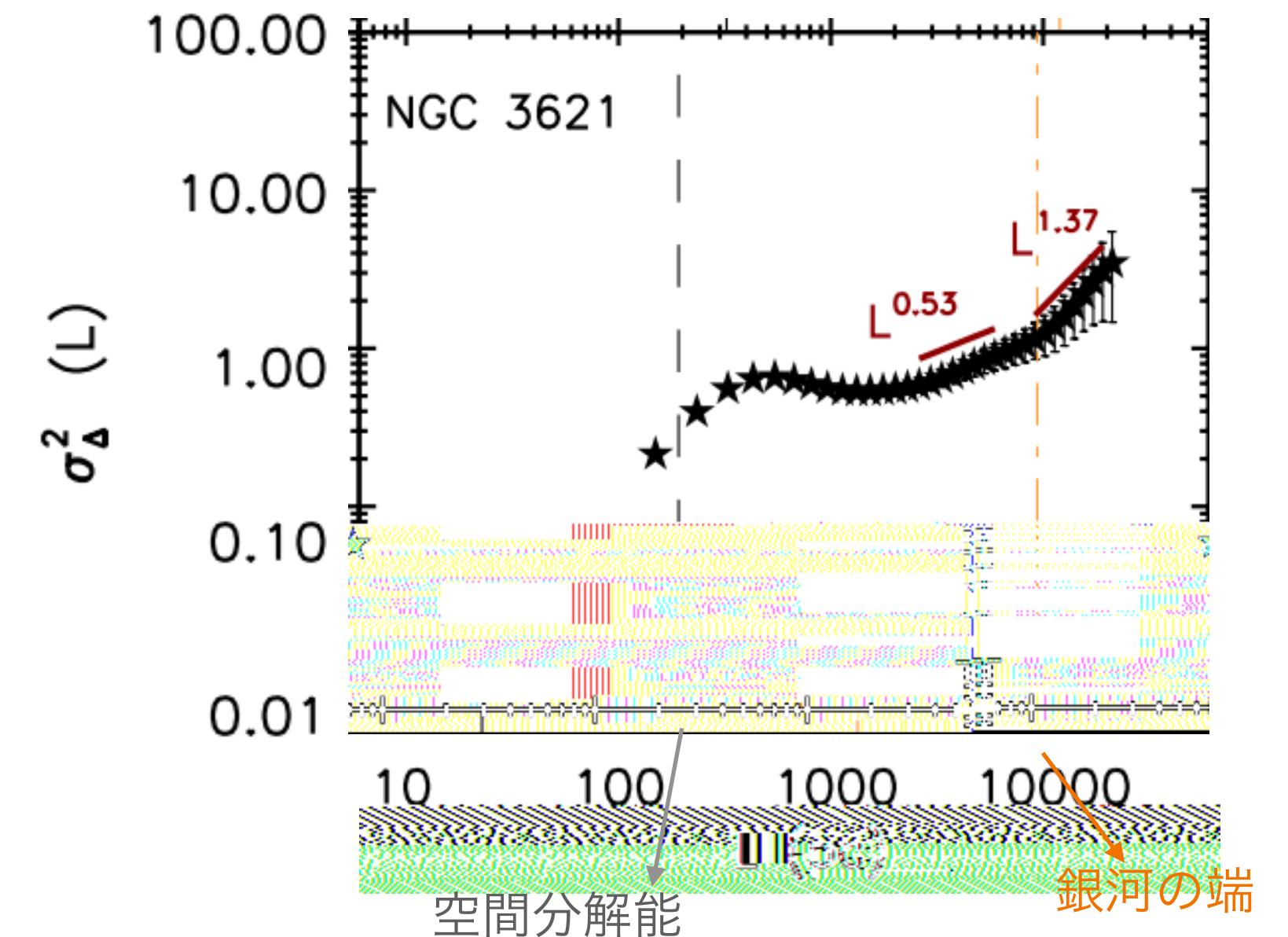
Sami Dib<sup>1</sup>, Jonathan Braine<sup>2</sup>, Maheswar Gopinathan<sup>3</sup>, Maritza A. Lara-López<sup>4</sup>, Valery V. Kravtsov<sup>5</sup>, Archana Soam<sup>6</sup>, Ekta Sharma<sup>3,7</sup>, Svitlana Zhukovska<sup>8</sup>, Charles Aouad<sup>9</sup>, José Antonio Belinchón<sup>10</sup>, George Helou<sup>11</sup>, Di Li<sup>12,13,14</sup>

銀河スケールでの星形成関係の論文

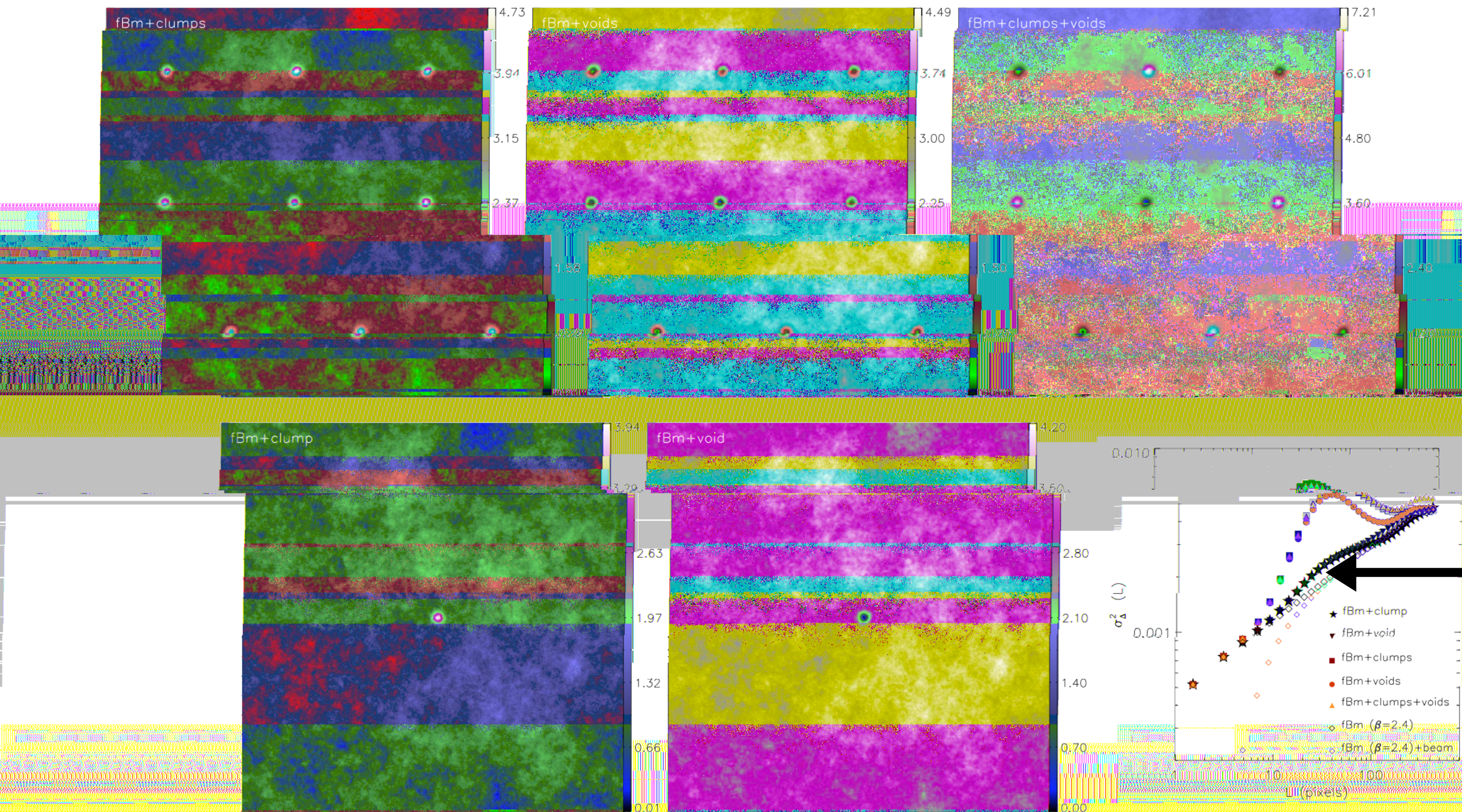
- ◆近傍銀河（33個）におけるHIガスの空間構造を、（ $\Delta$ 分散）スペクトルを用い定量解析した。（HI Nearby Galaxy Survey (THINGS)から抽出）
- ◆多くの銀河で、数パーセクから数百パーセクのスケールでスペクトルに盛り上がり（バンプがある）：この特徴的なスケールは、超新星爆発からのフィードバックの影響であると解釈する。
- ◆ほとんどの銀河で2つの自己相似的なスケールフリーの領域が観測された：小さいスケールでHIガスの冷たい相(CNM)の超音速乱流によって生成される部分と、大きいスケールでHIガスの暖かい相(WNM)に特徴的な亜音速から遷音速の乱流によって生成される部分と解釈。銀河の半径の半分くらいのスケールを境にしていた。

（ $\Delta$ 分散スペクトル：ある種のパワースペクトル）

解析の1例



Δ分散スペクトルのデモンストレーション.



fBm : fractal Brownian motion  
(特徴的なスケールのない構造の例)

fBmをバックグラウンドにして, 10 pixels 程度のボイドやクランプを人工的に配置.

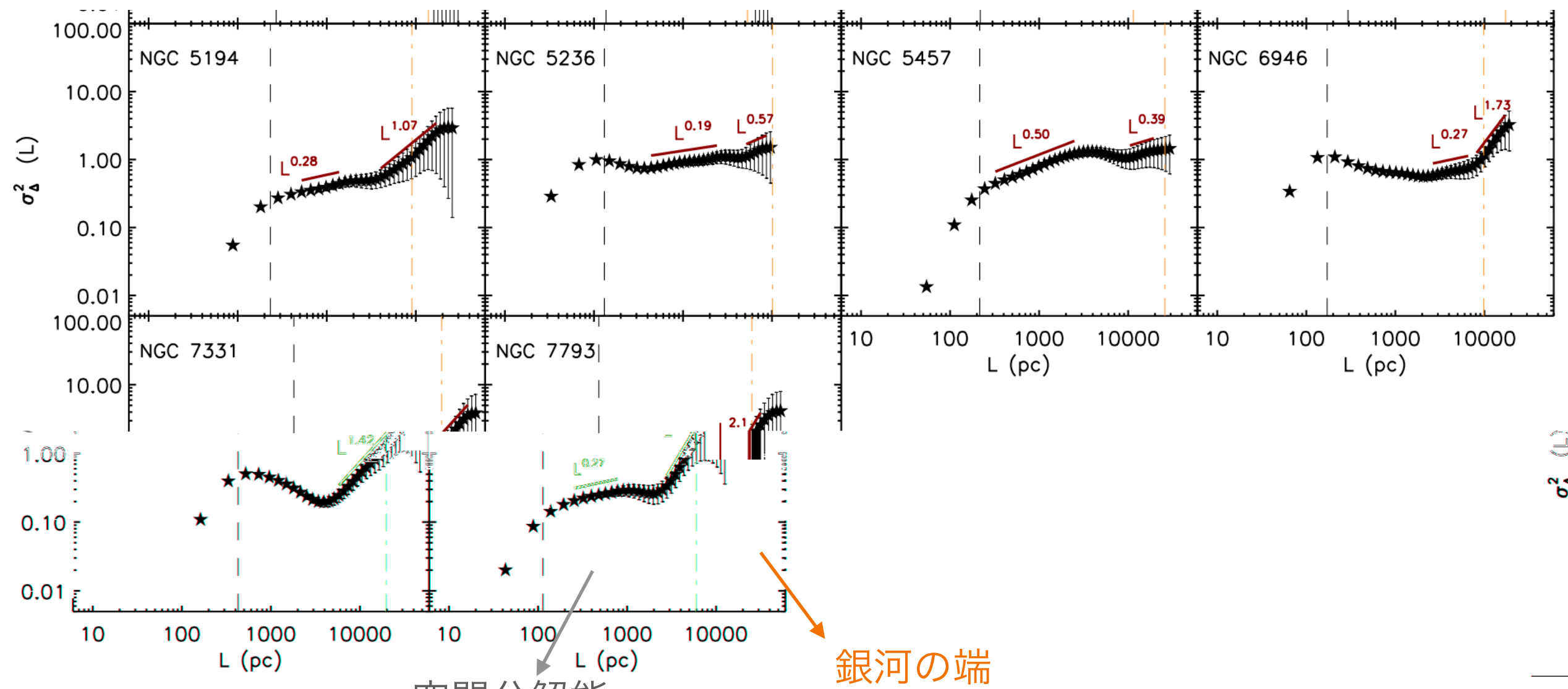
その時の Δ分散スペクトル.

ボイドやクランプが多いと, そのスケールでのスペクトルの盛り上がり (バンプ) が大きくなる.

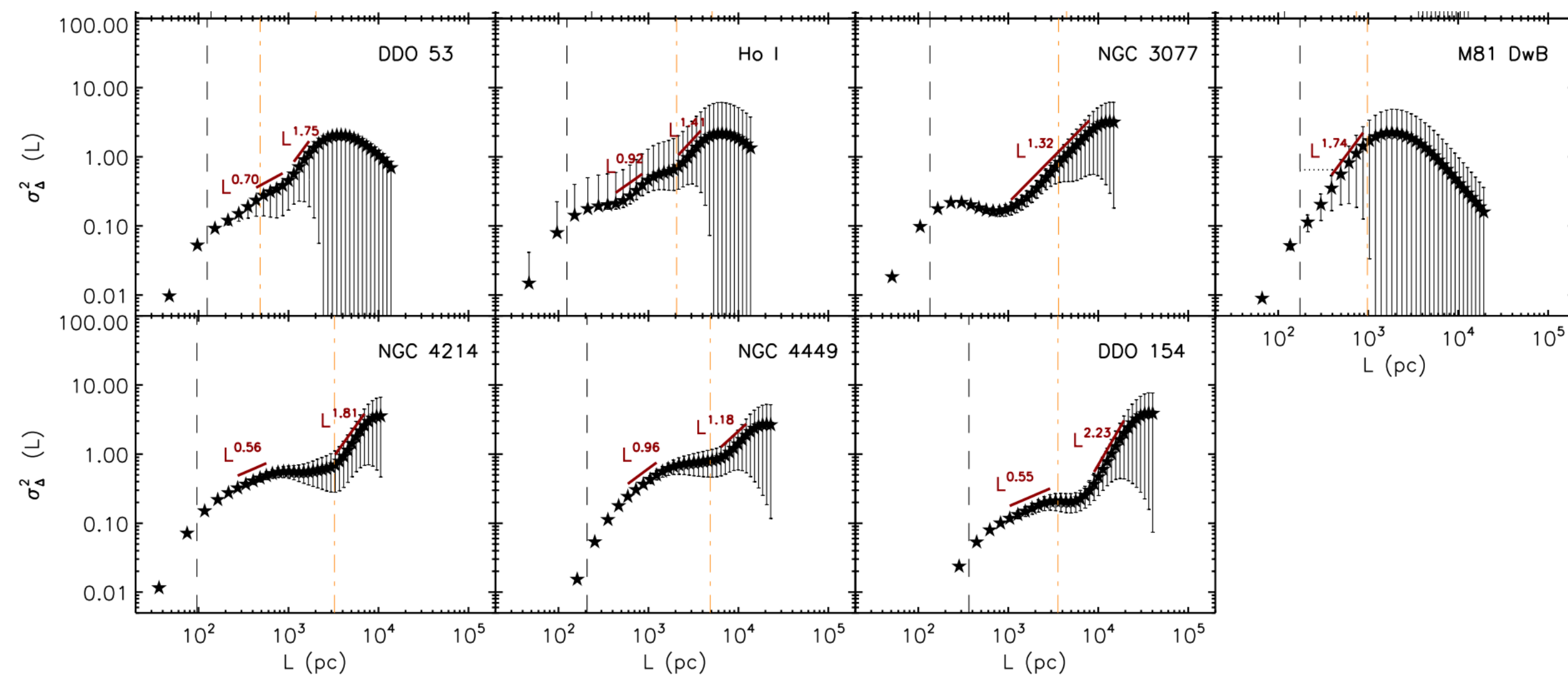
**Fig. 1.** 2D Gaussian structures injected on top of an fBm image with  $\beta = 2.4$ . The fBms are shifted to positive values by adding an arbitrary constant and normalized by their mean values. The maps have a resolution of  $1000 \times 1000$  pixels. The 2D Gaussian functions all have an aspect ratio of 1 ( $f = \sigma_1/\sigma_2 = 1$ ) and a contrast between the peak of the Gaussian and the mean value in the map of  $\delta_c = 3$ . The standard deviation of the Gaussians are  $\sigma_1 = \sigma_2 = 10$  pixels. All maps are normalized to their mean value. The maps correspond to the case of a single 2D Gaussian (left), a number of 2D Gaussians (top left), an inverted 2D Gaussian (bottom mid), a number of inverted 2D Gaussians (top middle), a mix of 2D Gaussians and inverted 2D Gaussians (top right). The corresponding  $\Delta$ -variance functions calculated for each case are displayed in the right subpanel, and they are compared to the  $\Delta$ -variance function of the underlying fBm image as well to the case of the same fBm smoothed with a Gaussian beam whose FWHM is 6 pixels.

# 解析結果の例

渦巻銀河 (全22個解析：下の図はその一部)



矮小銀河 (全11個解析：下の図はその一部)



銀河ごとに個性がある。  
大雑把のを見ると、以下の模式図のような共通点

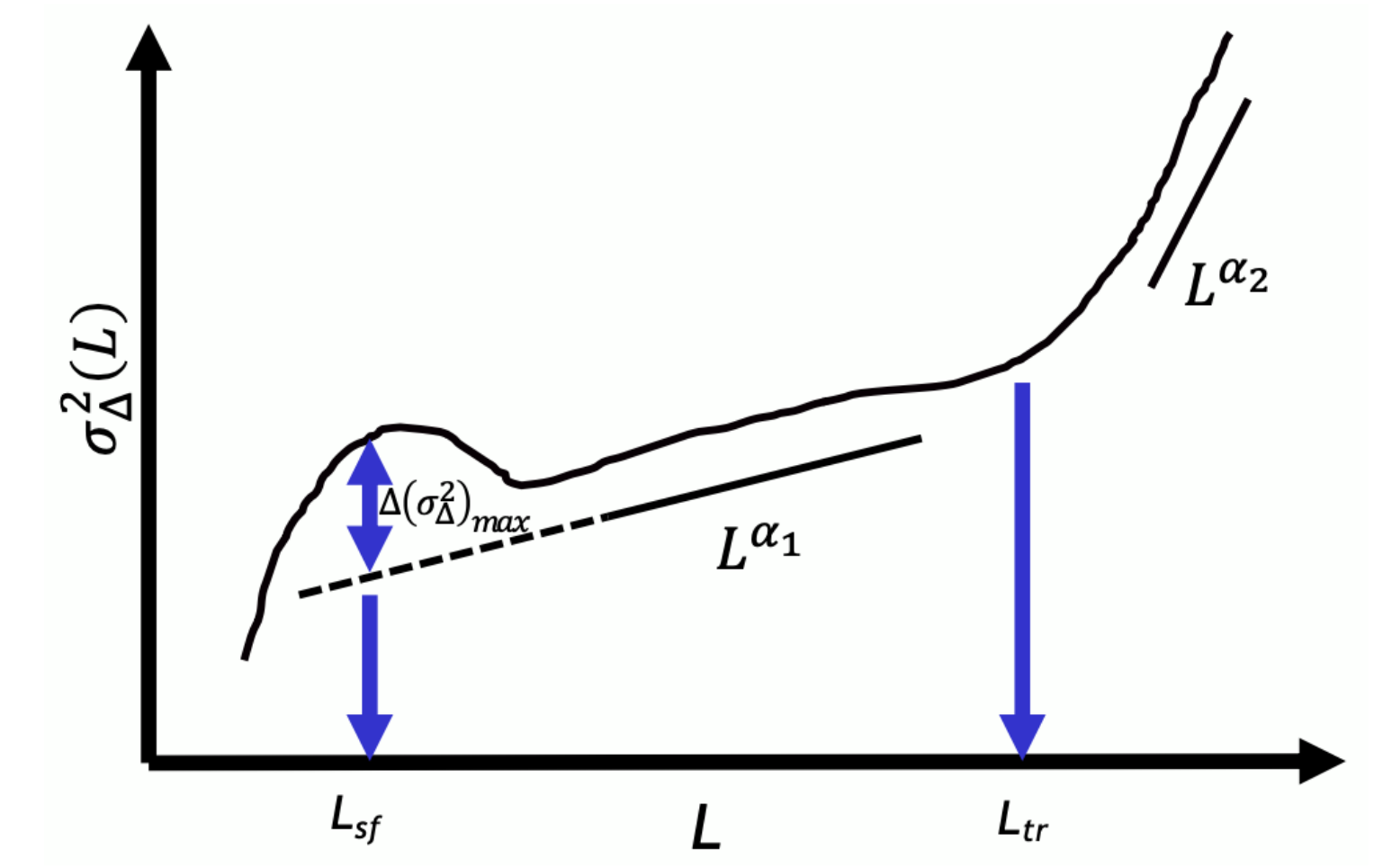
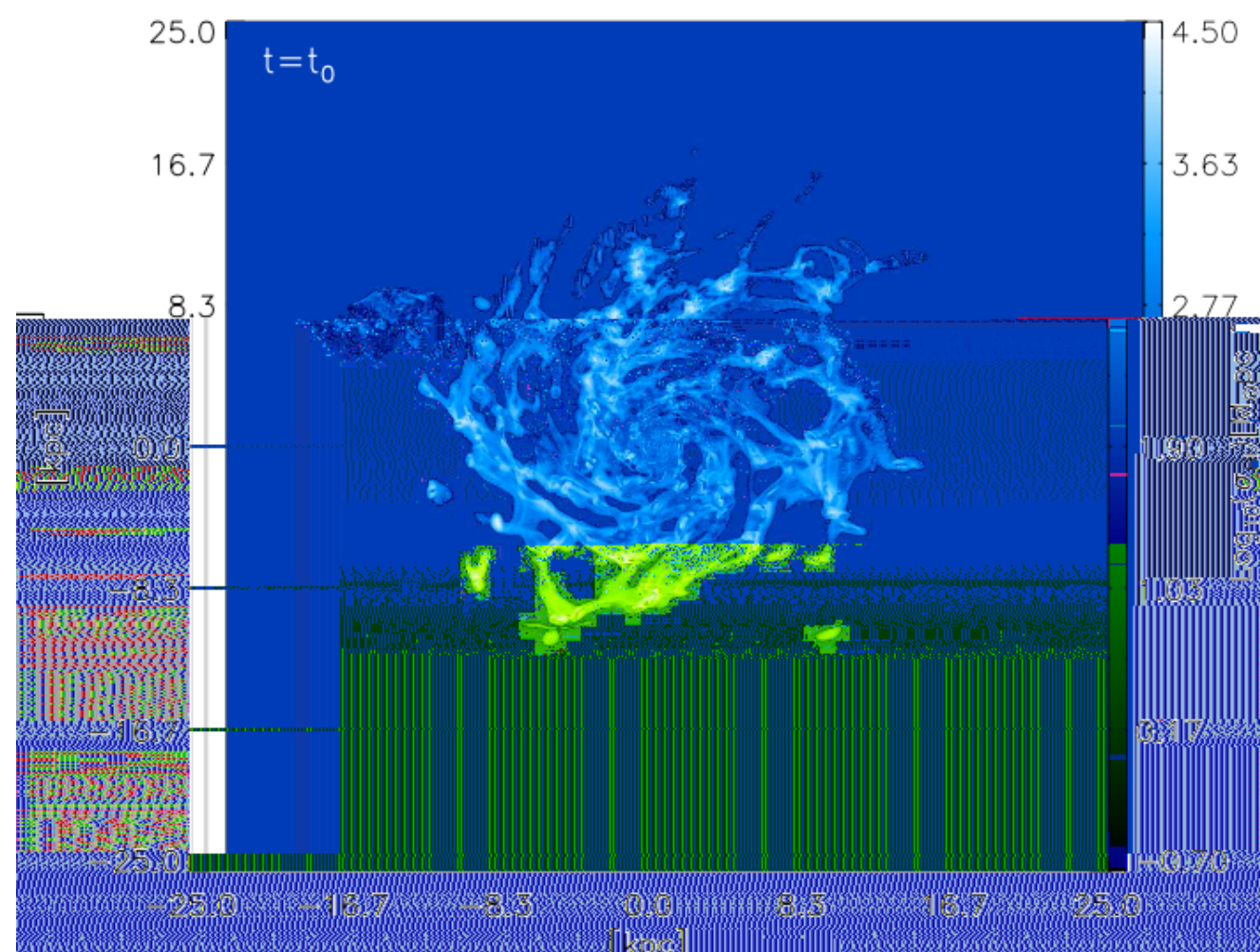


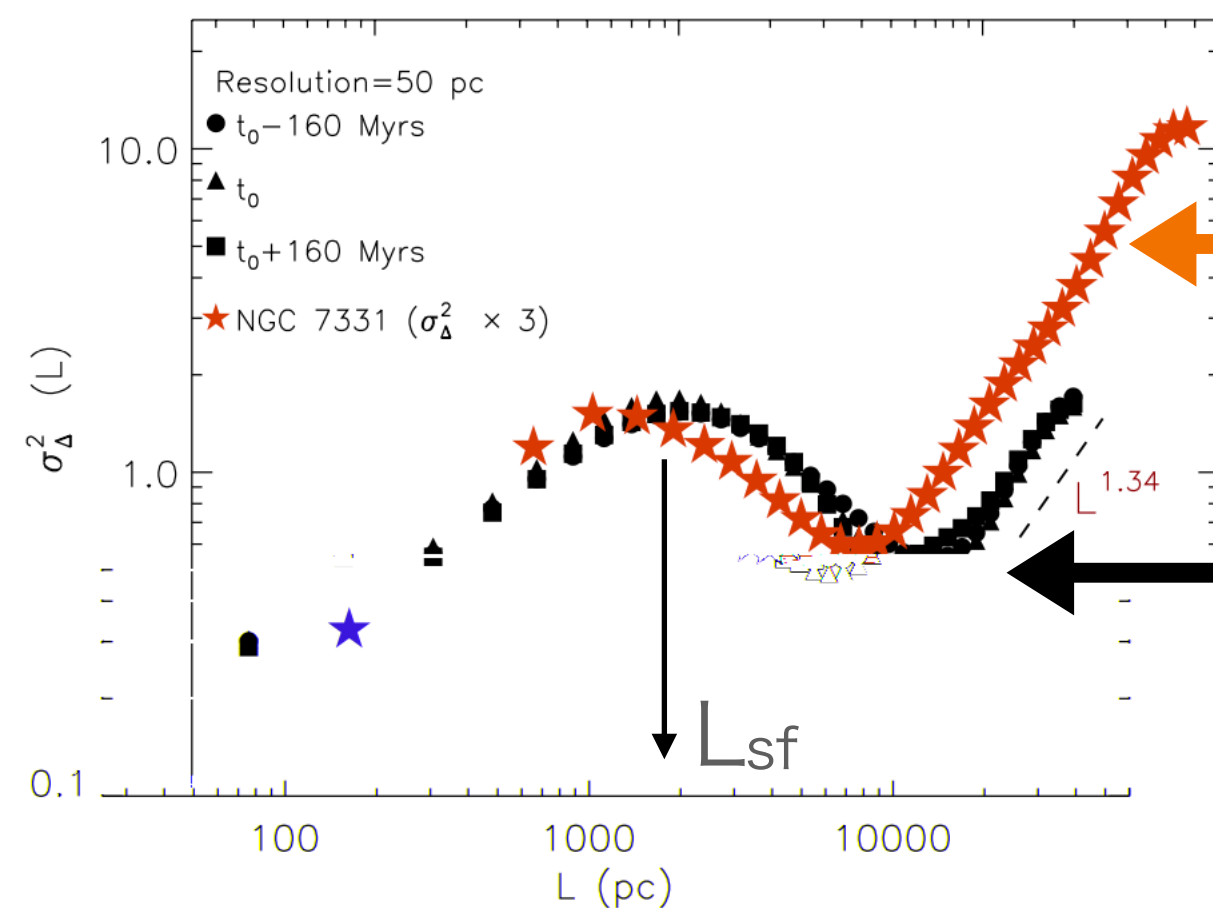
**Fig. 4.** Schematic figure representing the shape of the  $\Delta$ -variance spectrum for the THINGS galaxies. In some galaxies, some of the features of the spectrum such as the bump at small scales or the presence of two distinct power laws are not observed. The dashed line represents the extrapolation of the first power law down to smaller scales. The quantity  $\Delta(\sigma_{\Delta}^2)$  represents the maximum deviation between the bump and the extrapolated power law. The value of  $L_{sf}$  represents the physical scale at which this maximum deviation occurs. As illustrated, this scales does

# バンプについて

## 数値シミュレーションとの比較



- 銀河形成の数値シミュレーションの結果。(HIの面密度)
- 超新星爆発によるガスへのフィードバックによって、構造ができています。

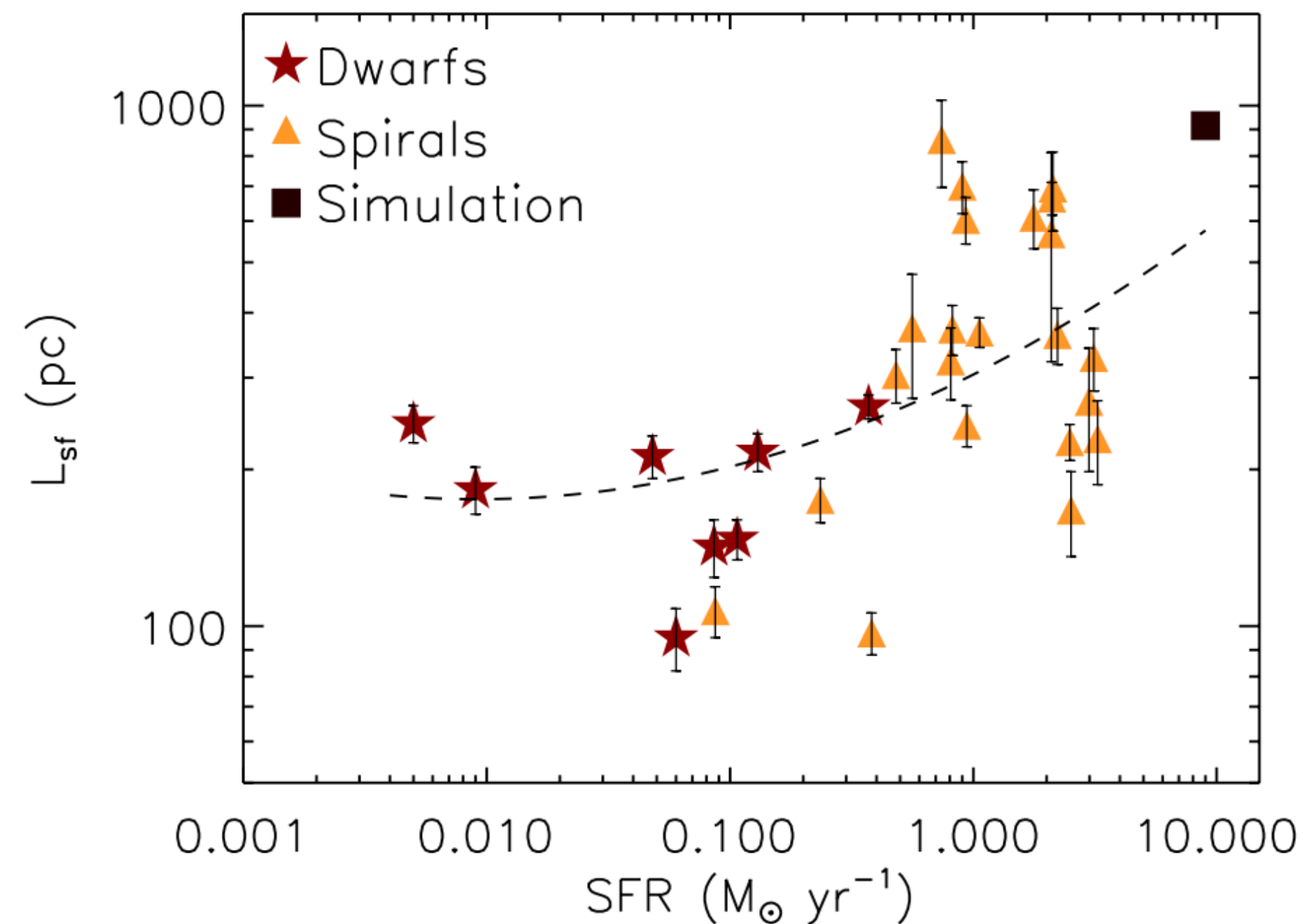


観測：NGC7331

数値シミュレーション

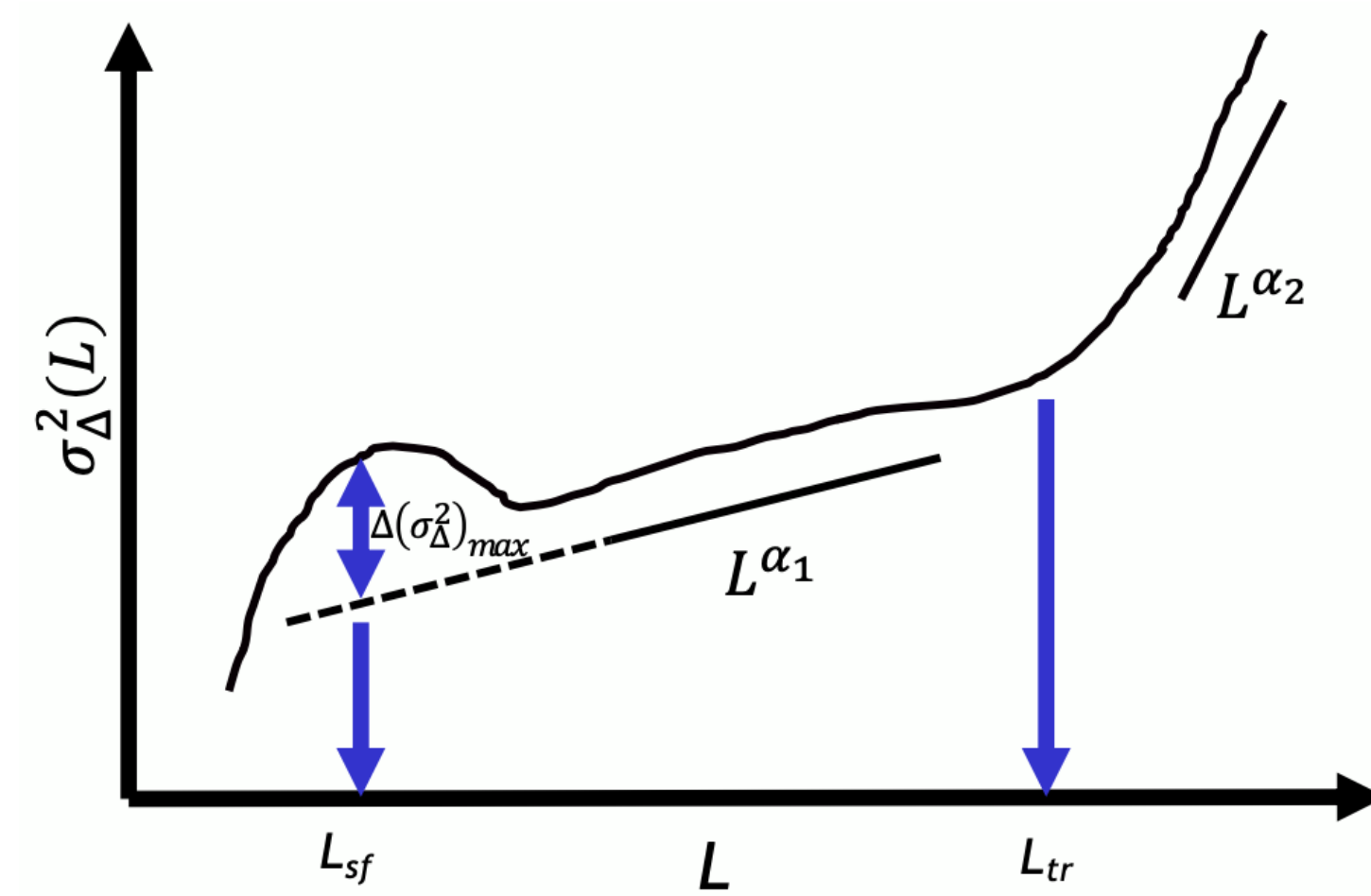
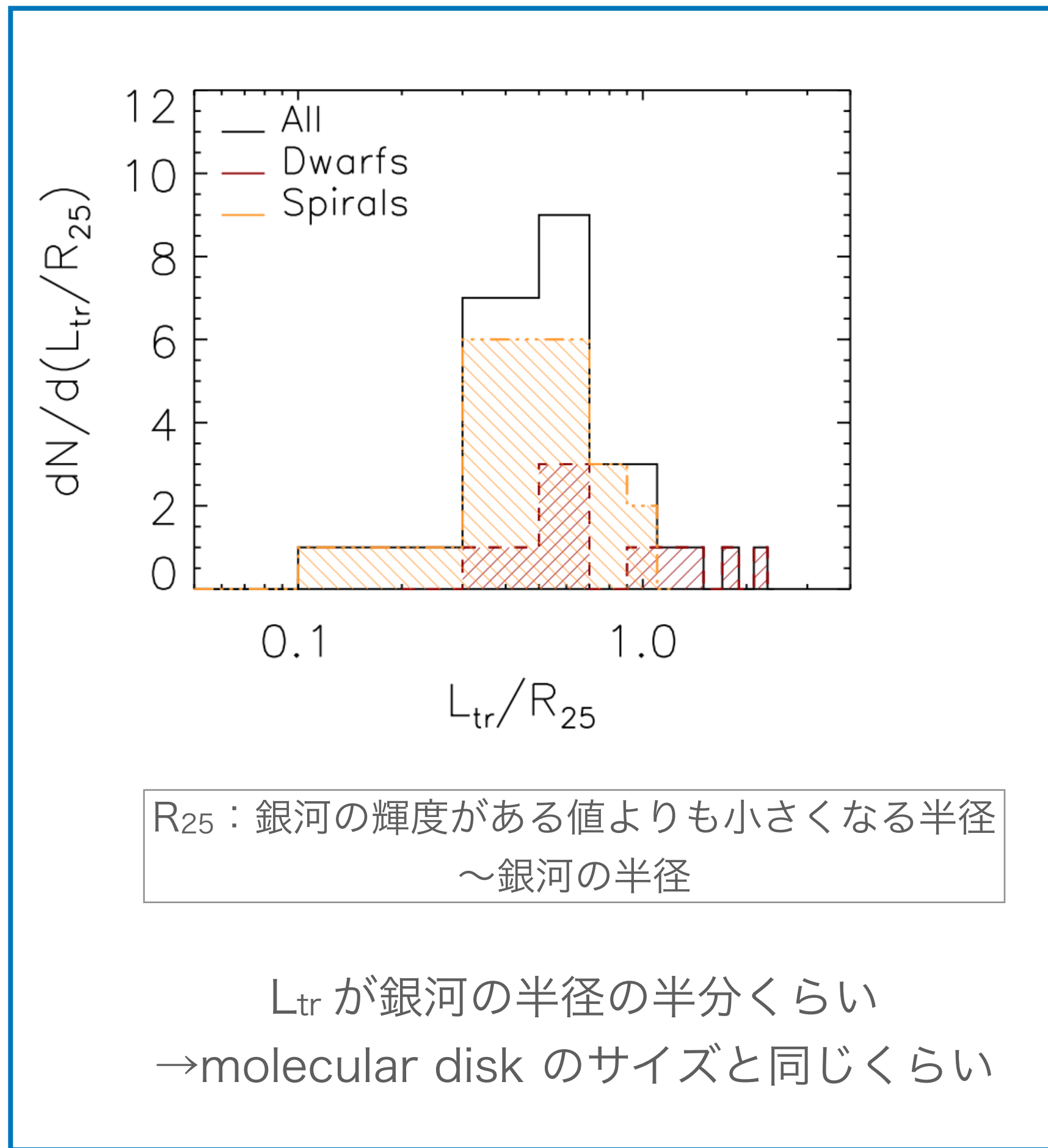
Fig. 8.  $\Delta$ -variance spectra of the simulated galaxy at different epochs. The spectra are calculated using the full resolution of the grid, which is 50 pc. The spectra are all normalized to their respective mean values. The models are compared to the case of the galaxy NGC 7331, where the  $\Delta$ -variance of NGC 7331 has been multiplied by a factor of 3. The dashed line shows a fit to the  $\Delta$ -variance spectrum of the models in the scale range [10 – 20] kpc and at  $t = t_0$ .

星形成率が高いと、バンプのスケールが大きくなる傾向がある



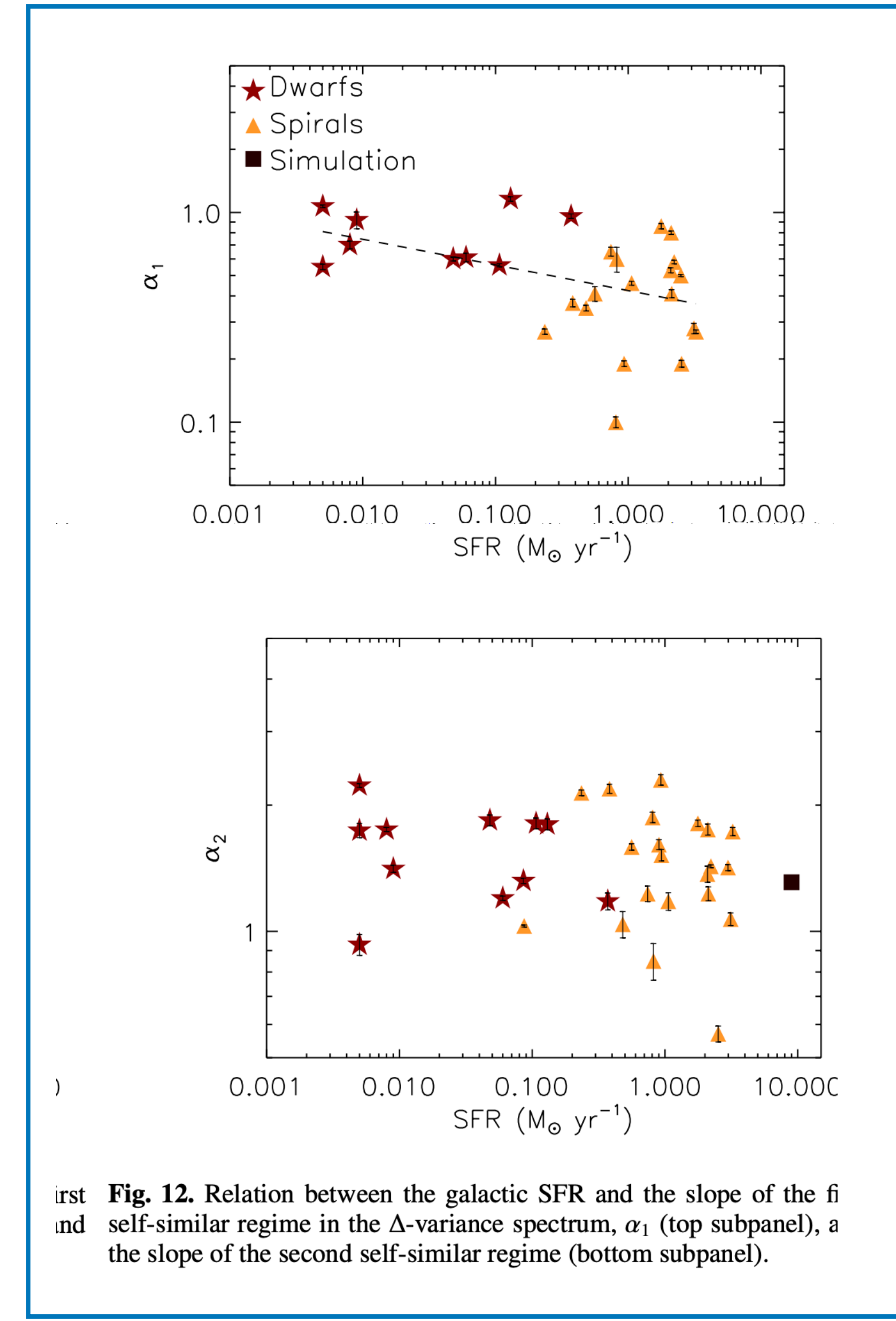
このバンプの構造は、超新星爆発からのフィードバックの影響であると解釈する。

二つの自己相似的なスケールフリーの領域について



- 小さいスケールは, HIガスの冷たい相(CNM)の超音速乱流
- $\alpha_1$ の平均値~0.5.
- SFRが大きくなると小さい  $\alpha_1$  (圧縮が支配)

- 大きスケールは, HIガスの暖かい相(WNM)の乱流
- SFRとの相関がない.



(2) 12 Tying the geometrical traits of massive young stellar objects and their discs to a potential evolutionary sequence using infrared observations

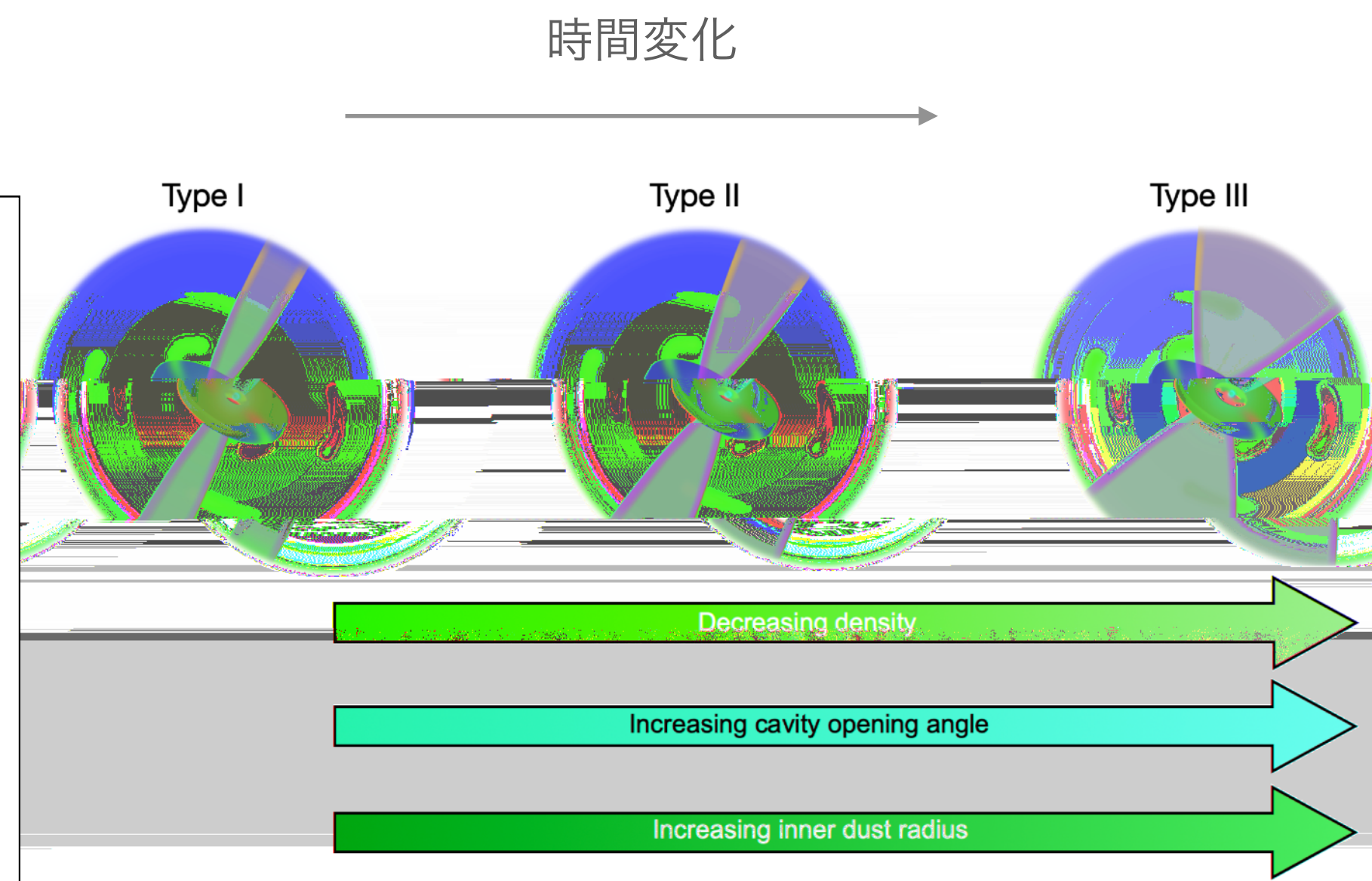
A. J. FROST <sup>1,2</sup> R. D. OUDMAIJER,<sup>2</sup> S. L. LUMSDEN,<sup>2</sup> AND W. J. DE WIT<sup>3</sup>

11

Unveiling the traits of massive young stellar objects through a multi-scale survey\*  
A. J. Frost<sup>1</sup>, R. D. Oudmaijer<sup>2</sup>, W. J. de Wit<sup>3</sup> and S. L. Lumsden<sup>2</sup>

動機：大質量のYSOの進化を観測で知りたい

- ◆大質量YSO (MYSO) の空間構造の解析 (彼ら独自) と, 他の観測から得られる進化段階との組み合わせから, MYSOの進化を調べた.
- ◆独自の解析から, 空間構造を得る.  
円盤+エンベロープ (アウトフローとキャビティ含む) モデルを作って Radiative Transferを解き, いくつかの観測結果を矛盾なく説明するような空間構造を得る (Frost et al. 2019)
- ◆大質量の原始星の周りでは,  $10^3-10^5$ 年で左図の模式図のように円盤が進化していることが示唆された.



大質量のYSOにおいても, 小質量星のClass0-IIと似たような, 進化を考えられる.

解析したMYSO

Name	RA (J2000) (h:m:s)	DEC (J2000) (d:m:s)	$\log(\frac{L}{L_{\odot}})$	Distance (kpc)
G305.20+0.21	13:11:10.45	-62:34:38.6	4.7 <sup>1</sup>	4.0 <sup>2</sup>
W33A	18:14:39.0	-17:52:03	4.5 <sup>3</sup>	2.4 <sup>4</sup>
NCC 2264 IRS1	06:41:10.15	+00:20:22.6	2.6 <sup>5</sup>	0.7 <sup>6</sup>
S255 IRS3	06:12:54.02	+17:59:23.60	4.7 <sup>7</sup>	1.8 <sup>8</sup>
IRAS 17216-3801	17:25:06.51	-38:04:00.4	4.8 <sup>9</sup>	3.1 <sup>10</sup>
M8EIR	18:04:53.18	-24:26:41.4	3.8 <sup>11</sup>	1.3 <sup>12</sup>
AFGL 2136	18:22:26.38	-13:30:12.0	5 <sup>1</sup>	2.2 <sup>13,14</sup>

**Table 2.** In this table we present the types of the sources we derive for the MYSOs of our sample and the ages we derive by comparing our cavity sizes to the work of Offner et al. (2011).  $\theta_{cav}$  is the cavity opening angle. The units of the line fluxes are  $\text{Wm}^{-2}\mu\text{m}^{-1}$ . For clarity, we also include the emission line information from Cooper (2013), Pomohaci (2017), Porter et al. (1998) and Cooper et al. (2013) used in the classification process and some relevant geometric information from our previous work, Frost et al. (2021), which we discuss in Section 4. The cavity opening angle of G305 is starred as this source has a secondary dusty source within its outflow cavity, which likely affected the fitting process. As a result, we do not calculate an age for this source. A full discussion can be found in Frost et al. (2019). The spectral information for M8EIR comes from Porter et al. (1998), where the line strength is presented relative to the flux of the Br $\gamma$ , so these ratios are reiterated for that source.

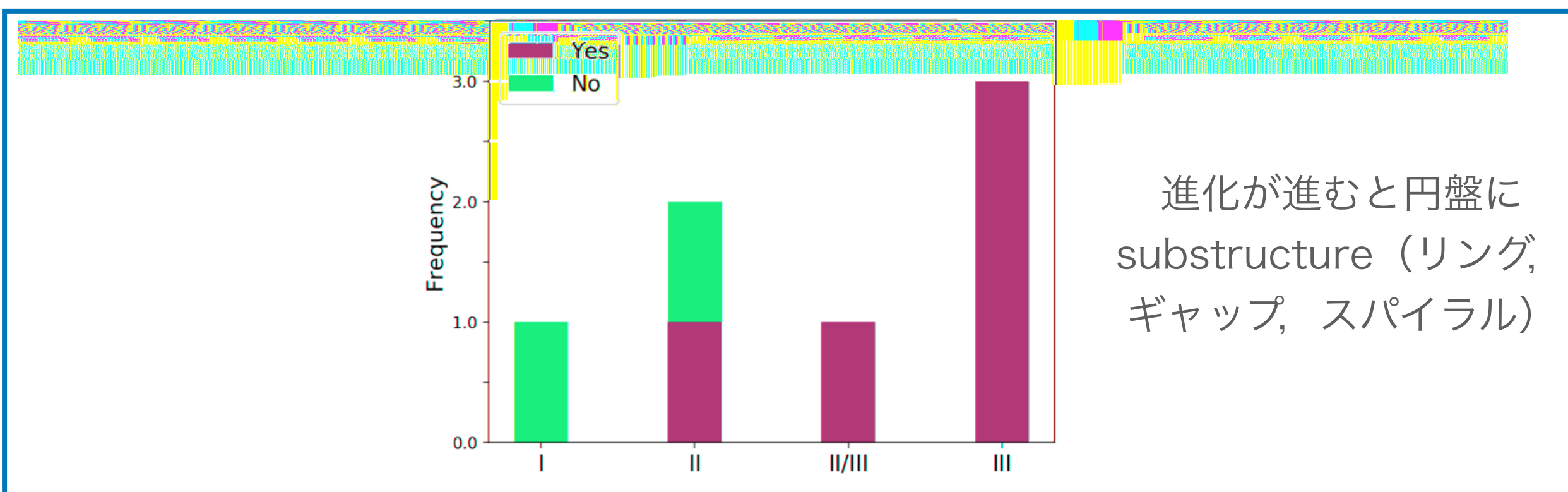
No line data are included for IRAS 17216-3801 as the emission lines were present in the differential phase and visibility of the spectrointerferometric data of Kraus et al. (2017). The non-detection of H $_2$  for AFGL 2136 is discussed in Section 2.

Name	$\log(\frac{L}{L_{\odot}})$	$\theta_{cav}$ ( $^{\circ}$ )	Cavity density ( $\text{gcm}^{-3}$ )	Type	H $_2$ flux	Br $\gamma$ flux	Br 10 flux	fl-FeII flux	Age (log yr)
W33A	18 ( $\sim R_{sub}$ )	20	$1 \times 10^{-19}$	II	$(8.7 \pm 0.1) \times 10^{-18}$	$(2.1 \pm 0.2) \times 10^{-17}$	-	-	3.1
G305.20+0.21	60 ( $\sim 3.5 R_{sub}$ )	12*	$1 \times 10^{-19}$	II	$(1.2 \pm 0.003) \times 10^{-17}$	$(1.1 \pm 0.002) \times 10^{-17}$	-	-	-
AFGL 2136	125 ( $\sim 4 R_{sub}$ )	22.5	$3 \times 10^{-19}$	II/III	-	$(2.9 \pm 0.1) \times 10^{-17}$	-	-	3.5
GC 2264 IRS1	4 ( $\sim R_{sub}$ )	25	$8 \times 10^{-21}$	III	$< 7.0 \times 10^{-16}$	$(9.9 \pm 0.3) \times 10^{-16}$	$(4.0 \pm 0.3) \times 10^{-16}$	$(1.8 \pm 0.3) \times 10^{-16}$	3.8
IRAS 17216-3801	100 ( $\sim 3 R_{sub}$ )	40	$9 \times 10^{-21}$	III	-	-	-	-	5.0
M8EIR	30 ( $\sim 1.5 R_{sub}$ )	25	$8 \times 10^{-21}$	III	-	1	0.37	0.06	3.8

天体の構造  
Frost et al. 2021

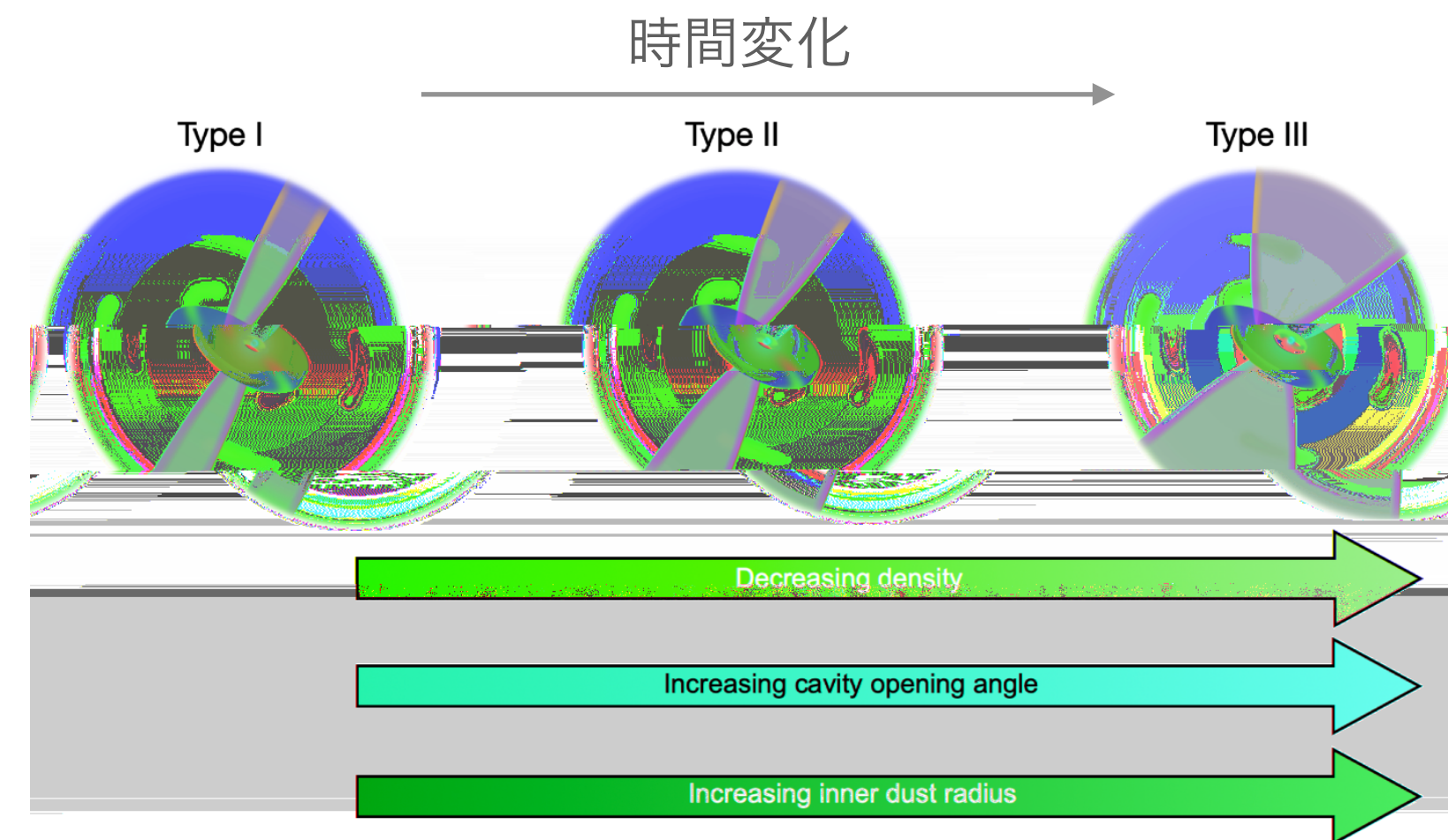
天体からの輝線 (Type分類)  
Cooper 2013 他

数値シミュレーション  
(Offner et al. 2011)  
とアウトフローの開き角  
( $\theta_{cav}$ )から推測



進化が進むと円盤に  
substructure (リング,  
ギャップ, スパイラル)

**Figure 2.** Histogram showing whether substructure is present with the MYSOs for each evolutionary type. Within this work we define substructure as a) a deviation from axisymmetry within the disc or 2) the expansion of the inner dust radius beyond the dust sublimation radius).



## 7. The GRAVITY Young Stellar Object survey. VII. The inner dusty disks of T Tauri stars

The GRAVITY Collaboration, K. Perraut et al. ★ These protoplanetary disks in T Tauri stars play a central role in star and planet formation. We spatially resolve at sub-au scales the innermost regions of a sample of T Tauri's disks to better understand their morphology and composition. We extended our homogeneous data set of 27 Herbig stars and collected near-IR K-band observations of 17 T Tauri stars, spanning effective temperatures and luminosities in the ranges of 4000-6000 K and 0.4-10 Lsun. We focus on the continuum emission and develop semi-physical geometrical models to fit the interferometric data and search for trends between the properties of the disk and the central star. The best-fit models of the disk's inner rim correspond to wide rings. We extend the Radius-luminosity relation toward the smallest luminosities (0.4-10 Lsun) and find the  $R \sim L^{(1/2)}$  trend is no longer valid, since the K-band sizes measured with GRAVITY are larger than the predicted sizes from sublimation radius computation. No clear correlation between the K-band half-flux radius and the mass accretion rate is seen. Having magnetic truncation radii in agreement with the K-band GRAVITY sizes would require magnetic fields as strong as a few kG, which should have been detected, suggesting that accretion is not the main process governing the location of the half-flux radius of the inner dusty disk. Our measurements agree with models that take into account the scattered light. The

ratio of the K-band size to the sublimation radius may be a proxy for detecting disks with silicate features in emission from disks with weak and/or no silicate features. When comparing inclinations and PA of the inner disks to those of the outer disks (ALMA) in nine objects of our sample, we detect misalignments for four objects.

YSOサーベイのシリーズもの. T Tauri 型星の内側にあるダスト円盤の観測.

## Steady-state accretion in magnetized protoplanetary disks

Timmy N. Delage, Satoshi Okuzumi, Mario Flock, Paola Pinilla, Natalia Dzyurkevich ★ [abridged] We present a 1+1D global magnetically-driven disk accretion model that captures the essence of the MRI-driven accretion, without resorting to 3D global non-ideal MHD simulations. The gas dynamics is assumed to be solely controlled by the MRI and hydrodynamic instabilities. For given stellar and disk parameters, the Shakura-Sunyaev viscosity parameter  $\alpha$  is determined self-consistently under the framework of viscously-driven accretion from detailed considerations of the MRI with non-ideal MHD effects (Ohmic resistivity and ambipolar diffusion), accounting for disk heating by stellar irradiation, non-thermal sources of ionization, and dust effects on the ionization chemistry. Additionally, the magnetic field strength is constrained and adopted to maximize the MRI activity. We demonstrate the use of our framework by investigating steady-state MRI-driven accretion in a fiducial protoplanetary disk model around a solar-type star. We find that the equilibrium solution displays no pressure maximum at the dead zone outer edge, except if a sufficient amount of dust particles have accumulated there before the disk reaches a steady-state accretion regime. Furthermore, the steady-state accretion solution describes a disk that displays a spatially extended long-lifetime

inner disk gas reservoir (the dead zone) accreting a few  $10^{-9} M_{\odot} \text{yr}^{-1}$ . By conducting a detailed parameter study, we find that the extent to which the MRI can drive efficient accretion is primarily determined by the total disk gas mass, the representative grain size, the vertically-integrated dust-to-gas mass ratio, and the stellar X-ray luminosity. A self-consistent time-dependent

model is used to study the coupling between gas, dust, and stellar evaporation in our framework. Our model is used to understand the formation of dead zones and their potential to trap dust particles.

1次元の原始惑星系円盤のモデル：MRIにより降着をモデルで取り入れたもの。

## 10. The statistical properties of protostellar discs and their dependence on metallicity

Daniel Elsender, Matthew R. Bate ★ We present the analysis of the properties of large samples of protostellar discs formed

in four radiation hydrodynamical simulations of star cluster formation. The four calculations have metallicities of 0.01, 0.1, 1

and 3 times solar metallicity. The calculations treat dust and gas temperatures separately and include a thermochemical model

of the diffuse interstellar medium. We find the radii of discs of bound protostellar systems tend to decrease with decreasing

metallicity, with the median characteristic radius of discs in the 0.01 and 3 times solar metallicity calculations being  $\approx 20$  and

$\approx 65$  au, respectively. Disc masses and radii of isolated protostars also tend to decrease with decreasing metallicity. We find that

the circumstellar discs and orbits of bound protostellar pairs, and the two spins of the two protostars are all less well aligned

with each other with lower metallicity than with higher metallicity. These variations with metallicity are due to increased small

scale fragmentation due to lower ionization and greater gas accretion rates with lower metallicity, which increase the stellar multiplicity, thereby

and increase dynamical interactions. We compare the disc masses and radii of protostellar systems from the solar metallicity

calculation with recent surveys of discs around Class 0 and I objects in the Orion and Perseus star-forming regions. The masses

and radii of the simulated discs have similar distributions to the observed Class 0 and I discs.

星団形成の数値シミュレーション

